The Meteoritical Society

Meteoritics & Planetary Science 61, Nr 9, 2269–2283 (2026)
doi: 10.1111/maps.70215

The first discovery of a shocked, metasomatised CV3 chondrule-fragment in a (Al,Cu)-bearing micrometeorite

Giovanna AGROSÌ[1]*, Paola MANZARI[2], Daniela MELE[1], Johan VILLENEUVE[3,4], Tiziano CATELANI[5], Mattew J. GENGE[6], and Luca BINDI[7]*

[1]Dipartimento di Scienze della Terra e Geoambientali, Università di Bari, Bari, Italy
[2]Agenzia Spaziale Italiana, Centro Spaziale Giuseppe Colombo, Matera, Italy
[3]Centre de Recherches Pétrographiques et Géochimiques, CNRS, Nancy, France
[4]Universite Paris-Cite, Institut de Physique du Globe de Paris, CNRS, Paris, France
[5]Centro di Servizi di Microscopia Elettronica e Microanalisi, Università di Firenze, Florence, Italy
[6]Department of Earth Science and Engineering, Imperial College London, London, UK
[7]Dipartimento di Scienze della Terra, Università di Firenze, Florence, Italy

***Correspondence**
Giovanna Agrosì, Dipartimento di Scienze della Terra e Geoambientali, Università di Bari, via E.Orabona, I-70125, Bari, Italy.
Email: giovanna.agrosi@uniba.it
Luca Bindi, Dipartimento di Scienze della Terra, Università di Firenze, Via La Pira 4, I-50121, Florence, Italy.
Email: luca.bindi@unifi.it

(Received 23 January 2026; revision accepted 15 July 2026)

Abstract–We report the discovery of the second (Al,Cu)-alloy–bearing micrometeorite, FB-A2, recovered from Mount Gariglione (southern Italy), representing the sixth such occurrence worldwide. Although chondritic in nature, FB-A2 differs markedly from previously described microspherules. It is a scoriaceous micrometeorite dominated by silicates and contains a relict clast composed of Mg-rich olivine and pyroxene phenocrysts set in a Fe-rich silicate matrix. The particle rim hosts fine aggregates of phosphates, magnetite, Ni-bearing magnetite, and sulfides, whereas the interior contains nepheline crystals. A 120 μm (Al,Cu)-alloy grain occurs at one corner of the particle. The porphyritic texture of the clast indicates a chondrule fragment—the first identified in an (Al,Cu)-bearing micrometeorite—while polyhedral sub-grain boundaries and metal–sulfide veins record shock metamorphism. Iron-rich alteration of relict silicates is consistent with high-temperature (<560 °C) metasomatism typical of CV3 chondrites and is supported by oxygen isotope compositions close to the Carbonaceous Chondrite Anhydrous Mineral Line. Brecciation of chondrule olivine suggests impact-induced fluid pressure excursions during early Solar System metasomatism, whereas impact melt enveloping elongate olivines indicates a later impact that introduced the (Al,Cu)-alloys. Overall, the texture, mineralogy, and isotopic composition of FB-A2 provide the most detailed constraints yet on the origin of (Al,Cu)-bearing micrometeorites and confirm a genetic link to the Khatyrka meteorite.

INTRODUCTION

In the last two decades, the discovery of meteorites and micrometeorites containing unusual Al- and Cu-alloys dispersed in a chondritic matrix has aroused great interest in the scientific community, which is questioning the origin of this unusual combination and the possible parent bodies. The unusual nature of these alloys is due to the contrasting geochemical behavior of their components. Copper is a moderately volatile chalcophile element, while aluminum is a highly refractory lithophile element. Specific extreme conditions are thus required to form these alloys (Suttle et al., 2019; Genge et al., 2025).

Up until now, only few examples of (Al,Cu)-bearing alloys within extraterrestrial materials have been reported (Agrosì et al., 2025; Bindi et al., 2025; Genge et al., 2025; MacPherson et al., 2013; Suttle et al., 2019). They show a broadly chondritic composition and have (Al,Cu)-alloys with different stochiometric ratios, from pure Al to pure Cu, with the prevalence of khatyrkite ($CuAl_2$), cupalite and stolperite (CuAl), and an unnamed phase with Cu_3Al_2 stoichiometry. The first discovery of this unusual assemblage occurred in the Khatyrka meteorite (MacPherson et al., 2013). This meteorite consists of detrital grains recovered from undisturbed fluvial clay layers in the Koryak Mountains (Chukotka, Russia). Khatyrka was classified as an oxidized-subgroup (Allende-like) CV3 carbonaceous chondrite, and it is notable for its unique natural quasicrystals. In detail, Khatyrka meteorite contains, besides crystalline (Al,Cu)-alloys, icosahedrite, $Al_{63}Cu_{24}Fe_{13}$ (Bindi et al., 2009, 2011), decagonite, $Al_{71}Ni_{24}Fe_5$ (Bindi et al., 2025), and an unnamed icosahedral phase (i.e., i-phase II), with composition $Al_{62}Cu_{31}Fe_7$ (Bindi et al., 2016; Hu et al., 2020).

Some years after the discovery of the Khatyrka meteorite, (Al,Cu)-metallic alloys were found in a cosmic microspherule, named KT01, recovered in the Nubian Desert of Sudan (Suttle et al., 2019). Oxygen isotopes of KT01 suggested a possible CR chondrite affinity (Ma et al., 2023); however, mixing with atmospheric gas during melting on atmospheric entry complicated its interpretation. Recently, new additional occurrences of unusual (Al,Cu) alloys in extraterrestrial material have been documented. A scoriaceous microspherule with CO-CV group affinity (FB-A1) was found on top of Mt. Gariglione, Catanzaro (Italy; Agrosì et al., 2025). This micrometeorite contains the first natural approximant of an icosahedral quasicrystal ($Al_{52}Cu_{31}Fe_{10}Si_7$). Another recent discovery was an unmelted coarse-grained particle with a CV3-like source, micrometeorite from Congo (NG-1; Genge et al., 2025). Finally, two new scoriaceous microspherules with chondritic affinity (NMM/L1 and NMM/L2) were found among the micrometeorites collected from urban rooftops in Norway (Bindi et al., 2025), belonging to the Project Stardust collection (Larsen, 2017). The increasing discovery of new Khatyrka-like (Al,Cu)-bearing micrometeorites suggests that these exotic alloys may be more widespread than previously thought.

The current consensus on the origin of the (Al-Cu) alloys is that these alloys formed in an exotic, differentiated environment early in the Solar System history and were subsequently incorporated into the Khatyrka-like host material through an intense impact event that modified their structure (Lin et al., 2017 and references therein). Regarding the exotic nature and origin of the precursors of the Al-Cu alloys, although an extrasolar source was initially hypothesized (Suttle et al., 2019), the most plausible theory suggests a complex origin involving impact mixing between a CV3 chondrite parent body and a projectile from the ureilite protoplanet, differentiated by desilication of an aluminous igneous protolith by hydrothermal activity under highly reduced conditions (Genge et al., 2025).

In this work, we report the discovery of a second micrometeorite containing Al-Cu alloys from Mt. Gariglione in southern Italy. This new micrometeorite, although having a chondritic nature, is significantly different from the previously studied microspherule (FB-A1; Agrosì et al., 2025) and adds new insights into the origin of this rare material.

MATERIALS AND METHODS

Sample

The sample studied here (hereafter FB-A2) was sent to us with the FB-A1 sample by an Italian amateur collector (Agrosì et al., 2025). Both micrometeorites were found in 2002, and the collection and recovery details have already been described by Agrosì et al. (2025). FB-A2 has been deposited in the collections of the Museo di Scienze della Terra of the University of Bari (Italy), under registration number 19/nm.

Micro-Computed X-Ray Tomography

To preserve the integrity of the sample, FB-A2 was initially analyzed by X-ray micro-CT with a Bruker SkyScan 1172 high-resolution μ-CT scanner equipped with a polychromatic microfocus X-ray tube at the Department of Earth and Geo-environmental Sciences, University of Bari Aldo Moro (Italy). The sample was scanned using a pixel size of 0.50 μm. A 79 kV X-ray source was used with a current of 131 μA. A total of 1127 absorption radiographs were acquired over a 360 rotation with an angular step of 0.32°. Beam hardening was reduced by the presence of a 0.5 mm Al-filter between the source and detector. The raw data were reconstructed into two-dimensional slice images using the Bruker's NRecon software. Corrections for the beam-hardening effect and ring artifacts were also applied during the reconstruction process. μ-CT data sets were visualized using Bruker's CTVox software.

Scanning Electron Microscopy

An initial non-destructive analysis was carried out with a Zeiss LEO scanning electron microscope, model

EVO-50XVP, at the Department of Earth and Geo-environmental Sciences, University of Bari Aldo Moro (Italy). The SEM is coupled with an X-max (80 mm^2) energy dispersive (ED) Silicon drift Oxford detector (Oxford Instruments) equipped with a Super Atmosphere Thin Window, operating at 15-kV accelerating potential and 500-pA probe current, 5-nm beam size, and 8.5-mm working distance. It has secondary (SE) and backscattered electron (BSE) detectors.

After the non-destructive investigation, the sample was embedded in epoxy, polished, and studied with the aforementioned instrument and also with a Zeiss EVO MA15 scanning electron microscope at the Centre for Electron Microscopy and Microanalysis (MEMA) of the University of Florence (Italy). The SEM is coupled with an Oxford UltimMax 40 energy-dispersive spectrometer (EDS), operating at 15-kV accelerating potential and 700-pA nominal current in focused beam mode, for EDS mapping and spectra acquisition (30-s live time). For linescan analyses, the instrument was set up at 10-kV acceleration voltage and 500-pA nominal probe current (20 s dwell time for each point). The sample was sputter-coated with a 30-nm-thick carbon film.

Electron Backscattered Diffraction

Analyses were performed using a high-performance CMOS Oxford Symmetry S2 EBSD system working on a ZEISS EVO 15-MA SEM, operating at 15-kV and 9-nA nominal current in focused beam mode with a 70° tilted stage. EBSD patterns for phase identification and analysis were acquired with maximum pixel resolution (1244 × 1024). Cell constant was obtained by matching the experimental EBSD patterns to those of known synthetic phases. Before the analyses, the sample was gently repolished and sputter-coated with a 5-nm-thick carbon film.

Electron Microprobe

The same polished sample was then studied using a JEOL 8200 electron microprobe (WDS mode, 12 kV and 5 nA, focused beam) at the University of Florence (Italy). The focused electron beam is ~150 nm in diameter. Analyses were processed with the CITZAF correction procedure. All the elements were analyzed using Astimex standards.

Secondary Ion Mass Spectrometry

Oxygen isotope analyses were carried out using a CAMECA IMS 1270 E7 at the Centre de Recherches Pétrographiques et Géochimiques (Nancy, France). $^{16}O-$, $^{17}O-$, and $^{18}O-$ ions produced by a Cs^+ primary ion beam ($\sim$10 μm and $\sim$2 nA) were detected in multicollection mode using two off-axis Faraday cups (FCs) for $^{16}O-$ and $^{18}O-$ and the axial FC for $^{17}O-$. To remove the $^{16}OH-$ interference on the $^{17}O-$ peak and to obtain maximum flatness on the top of the $^{16}O-$ and $^{18}O-$ peaks, entrance and exit slits were adjusted to acquire a mass resolving power (MRP) of ≈7000 for $^{17}O-$ on the central FC. The multicollection FCs were set on slit 1 (MRP = 2500). The total measurement time was 180 s (150-s measurement +30-s pre-sputtering). We used four in-house terrestrial standard materials (SCOL San Carlos olivine, CAF magnetite, BHVO basaltic glass, and JV1 diopside) to (i) define the instrumental mass fractionation line for the three oxygen isotopes and (ii) to correct the instrumental mass fractionation due to the matrix effect in samples. Typical count rates obtained on the San Carlos olivine standard were 1.7×10^9 cps for ^{16}O, 6.5×10^5 cps for ^{17}O, and 3.5×10^6 cps for ^{18}O. The 2σ errors were ≈0.25‰ for $\delta^{18}O$, ≈0.35‰ for $\delta^{17}O$, and ≈0.4‰ for $\Delta^{17}O$ ($\Delta^{17}O$ representing the deviation from the TFL, $\Delta^{17}O = \delta^{17}O - 0.52 \times \delta^{18}O$).

RESULTS

Non-Destructive Analyses

A first optical examination of FB-A2 reveals it has a different shape (Figure 1) from FB-A1 (Agrosì et al., 2025). FB-A1 is a scoriaceous, elongated, subspherical micrometeorite, whereas FB-A2 is of an irregular shape. Both the samples show portions with an unusual metallic luster. In detail, FB-A1 showed metallic droplets extruded on the surface (Agrosì et al., 2025), whereas FB-A2 chiefly exhibits a facetted grain on one corner with a "silvery" metallic luster (Figure 1a,b).

The X-ray micro-CT analysis, performed on the whole sample, shows that the different colors highlight the phases with distinct X-ray attenuation coefficients (Figure 1c and Video S1). In particular, the red color corresponds to the phases characterized by the higher X-ray absorption (Figure 1c). They appear distributed in the whole sample, even if the similar attenuation coefficient of (Al,Cu)-metallic alloys and the other iron-rich phases (oxides, sulfides, metallic alloys) makes them indistinguishable. A 3D reconstruction of the whole sample (see the Video S1) shows the presence of voids and allows the porosity of the fragment to be determined. The region corresponding to the corner of (Al,Cu)-metallic alloys, named FB-A2a, exhibits different porosity with respect to the remanent portion of the sample, named FB-A2b. The FB-A2a region shows higher porosity (20.06%) than the FB-A2b (1.46%). The porosity of FB-A1 (Agrosì et al., 2025) was also

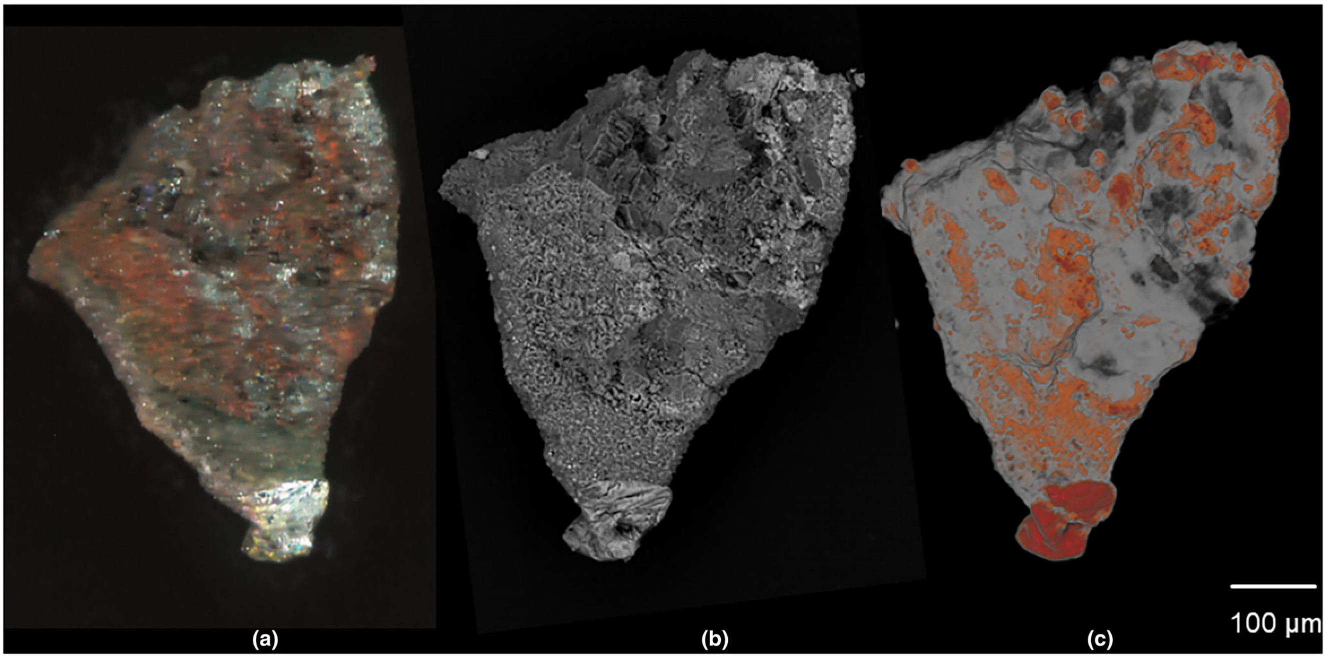

FIGURE 1. FB-A2 (a) optical image of micrometeorite. Note the corner with silver luster; (b) SEM-BSE image; (c) μ-CT 3D reconstruction. Note the red and orange particles corresponding to the metallic alloys. (Color figure can be viewed at wileyonlinelibrary.com)

calculated, and all the data were compared: the porosity of FB-A2a is very similar to the porosity measured on the FB-A1 microspherule. In both cases, they consist mainly of open pores (vesicles) (see Table 1 in supplementary material). The presence of the (Al,Cu)-metallic alloys is related to a high porosity: the percentage of closed and open voids of region FB-A2a is higher than that of FB-A2b and, in turn, the porosity of FB-A2a results very similar to that of FB-A1.

Preliminary SEM-EDS analyses on the uncoated and unpolished sample indicated a mineralogical assemblage similar to FB-A1, consisting of Fe-Ni alloys with variable composition, Fe-Ni sulfides, and oxides of the spinel group disseminated into a silicate-dominated matrix. Energy-dispersive spectroscopy analyses were performed on the metallic corner and its contact with the silicate region and reveal that the region with metallic luster corresponds to (Al,Cu)-alloys with variable composition (Figure 2a (BSE image) and Figure 2b (chemical map)). In particular, worm-like intergrowths of nearly pure Al (Cu-bearing aluminum) immersed in a matrix made of khatyrkite ($CuAl_2$) can be observed (Figure 2c). At the contact between the silicate matrix and the (Al,Cu)-metal, micrometric sub-spherical droplets of Fe-Ni alloys with variable composition (from awaruite to kamacite) can be observed. The inner part of these droplets exhibits voids, suggesting melting and degassing processes of precursor grains, likely sulfides (Figure 2c,d). It is worth noting the presence of cracks radiating from the central voids that separate droplet portions characterized by different Fe/Ni ratios.

Analyses on Polished Surface

Unfortunately, during the polishing of FB-A2, the (Al,Cu)-metallic phase at the corner of the fragment was lost. The bulk composition obtained by wide-beam analyses (Table 1) is broadly chondritic, even if the composition is slightly different from that of FB-A1. The differences mainly concern the depletion of Al and Cu (1.01 wt% of Al and Cu% below the detection limit) in FB-A2 due to the loss of the (Al,Cu)-metal at the corner. Also, FB-A2 shows a lower content of Fe, Ca, and O and a higher content of Mg and Si with respect to FB-A1, as well as small amounts of Na (0.21 wt%), which is completely absent in FB-A1.

The BSE image of the polished surface shows a heterogeneous texture, confirming μ-CT data (Figure 3a). The polished surface can indeed be divided into two main portions: the first portion (white dashed circle in Figure 3) corresponds to FB-A2a and appears made chiefly up of an amorphous material, with many vesicles and voids; the remanent portion (FB-A2b) shows clasts with porphyritic texture characterized by relict heterogeneous silicate crystals. Chemical maps reveal that FB-A2 is characterized by a moderate volatile depletion with a very low content of Na and S (Figure S2). Nevertheless, FB-A2 shows in the central part the

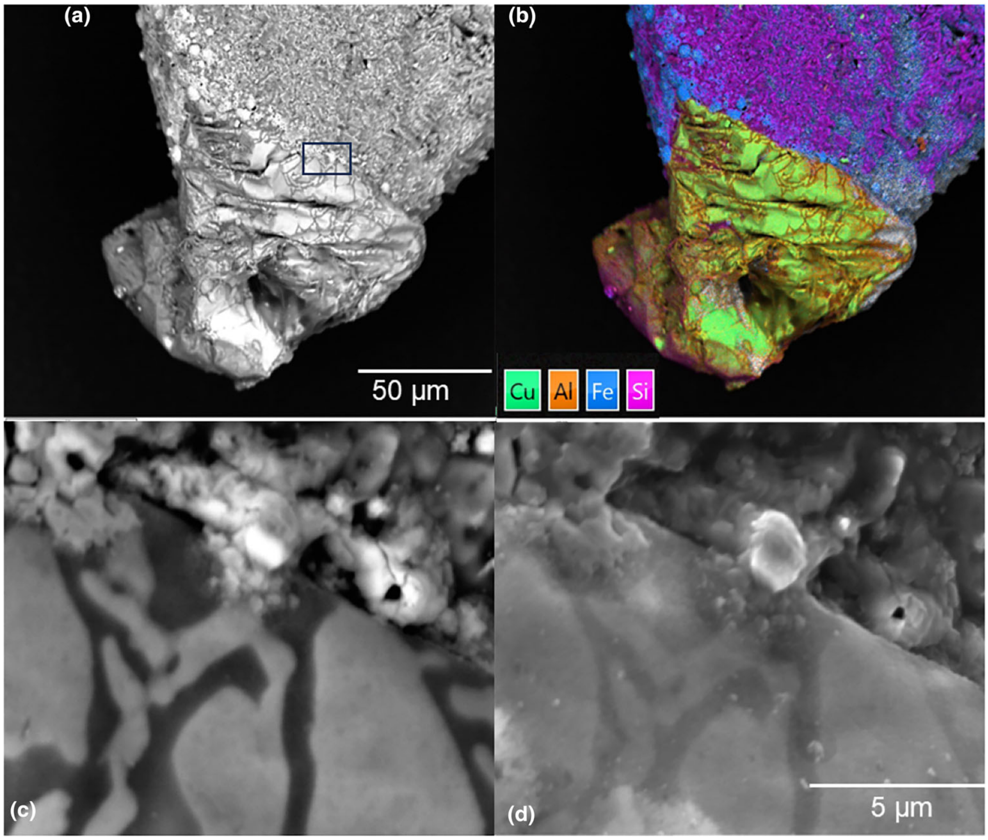

FIGURE 2. FB-A2 (a) BSE image of contact between /Al/Cu) alloys and chondritic matrix. Note the square corresponding to the enlarged detail shown in (c) and (d); (b) multilayered EDS maps of the same region of a); (c) BSE image of the enlarged detail of the portion surrounded by square in (a); (d) SE image of the same region of (c). Note worm-like dark contrasts consist of $Al_{75.26\%}Cu_{18.13\%}$ in Khatyrkite and the Fe/Ni subspherical particles with the central voids. (Color figure can be viewed at wileyonlinelibrary.com)

TABLE 1. Bulk analysis (wt% of elements) of FB-A2 and FB-A1 taken on polished surfaces by SEM-EDS wide beam.

Area	O	Na	Mg	Al	Si	P	S	Ca	Cr	Fe	Ni	Cu	Total
FB-A1	57.7	–	13.7	5.1	12.3	0.2	0.1	1.1	0.2	7.9	0.3	1.4	100
FB-A2	37.0	0.2	16.0	1.0	1618	0.1	0.1	0.0	1.1	0.1	0.5	–	100

Note: Analyses have been renormalized to 100%.

presence of nepheline (Nph), which is disseminated and surrounded by matrix (Figure 3a). The matrix consists of a Mg/Fe-rich silicate glass with olivine composition (Fo_{43}). Silicate phenocrysts, disseminated into the matrix, consist of relict olivine (Fo_{89}), chemically zoned with forsteritic core ($Fo_{99.9}$) and a rim characterized by an enrichment of iron (Fo_{78}) (Table 2). There are also pyroxene crystals that consist mainly of enstatite and Ca-rich clinopyroxenes ($En_{66.8}$, $Wo_{31.6}$) (Table 3). Some areas of the matrix contain elongate olivine crystals up to 36 μm in length and have interstitial void space (Figure 3c). The cores of these crystals have lower backscattered electron potentials and are likely to be more magnesian than their rims.

The clast (FB-A2b) comprises 56 vol% of the particle, is 400 by 225 μm in size and dominates one side of the particle, although a selvage of fine-grained matrix is present on its outer-surface. It has a porphyritic texture and consists of subhedral to euhedral crystals of forsteritic olivine and Mg-rich pyroxene up to 110 μm in length, with 70 vol% olivine and 22 vol% pyroxene. Areas of interstitial glass are present and represent 8 vol % of the clast. Both olivine and pyroxene crystals exhibit normal zoning with the outer margins of the crystals

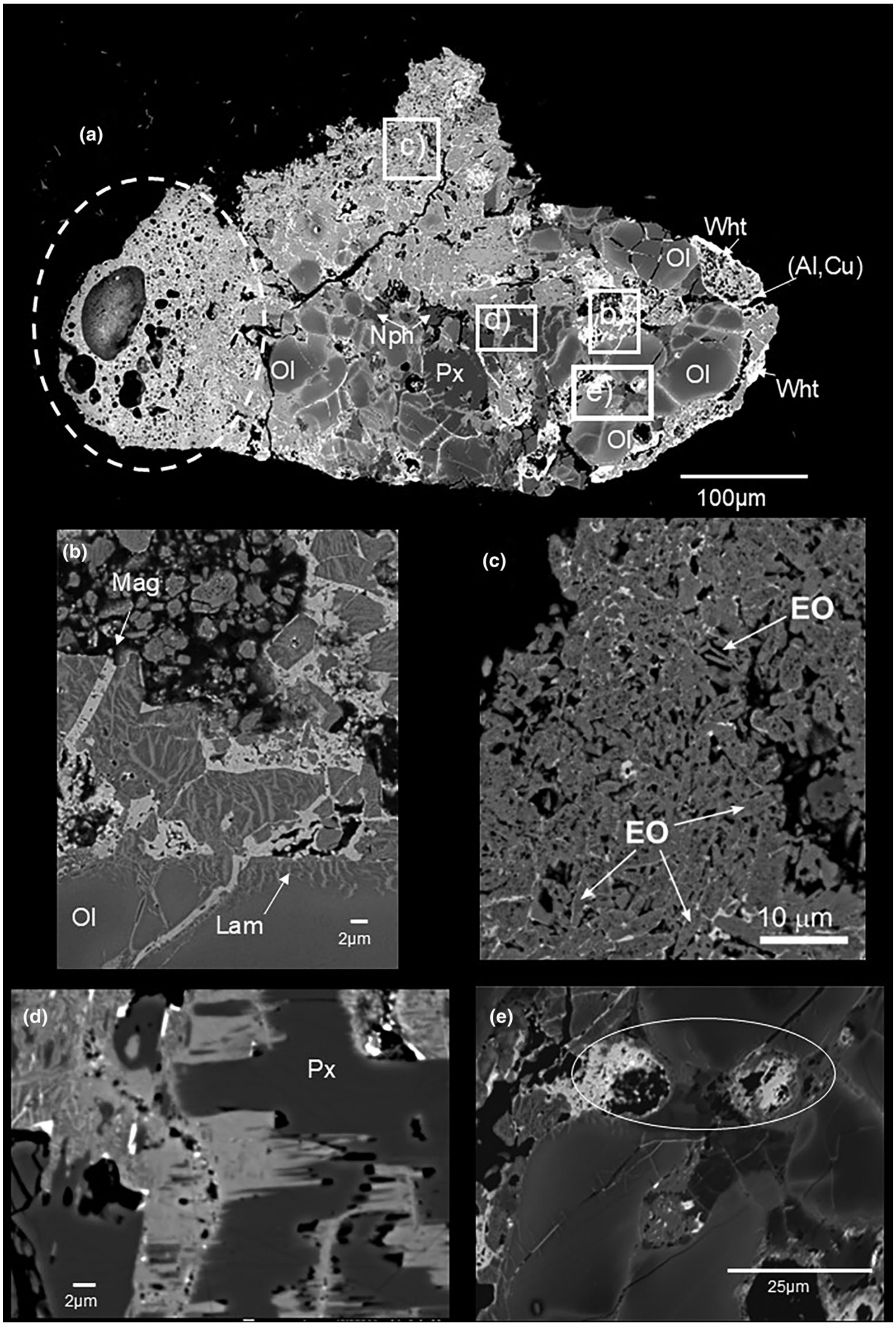

FIGURE 3. FB-A2 (a) BSE image of polished surface. The white dashed circle surrounds the region previously covered by (Al, Cu) alloys (FB-A2a). Note the phenocrysts in the clast (FB-A2b): relict Mg-rich olivine (Ol), pyroxenes (Px), nepheline (Nph), withlockite (Wht) and tiny crystals of (Al,Cu) alloys. The squares named (b)–(e) correspond to the enlarged details shown in Figure 3b–e, respectively. (b) Brecciated region showing a rim on olivine (Ol) with lamellae (Lam) of fayalitic olivine. Magnetite (Mag) forms the matrix of the breccia and as drusy layers in veins, (c) elongate olivines (EO) disseminated in the matrix in the upper part of the sample; (d) note the iron-rich olivine penetrates the pyroxenes (Px) forming parallel lamellae; (e) the white ellipse surrounds two cavities containing small and finely aggregated crystals of phosphates, magnetite, Ni-bearing magnetite and sulfides (pentlandite), in the inner part of brecciated region (FB-A2b).

TABLE 2. Chemical analyses (wt% of oxides) of the silicate phenocrystals and the matrix (EPMA-WDS or SEM-EDS).

	AVG [*n.* spots] (SD)	SiO_2	TiO_2	Al_2O_3	Cr_2O_3	FeO	MnO	NiO	MgO	CaO	Na_2O	K_2O	Total
Ol (Rel) Fo_{89}	EPMA [15]	40.91	0.04	–	0.06	10.69	0.16	0.03	48.79	0.20	–	–	100.90
		(0.51)	(0.01)		(0.03)	(2.45)	(0.01)	(0.01)	(2.21)	(0.03)			
Ol (Rel Rim) Fo_{78}	EPMA [7]	40.30	0.04	–	0.07	13.55	0.16	0.06	46.76	0.18	–	–	101.14
		(0.24)	(0.02)		(0.07)	(1.44)	(0.01)	(0.02)	(1.35)	(0.02)			
Ol (Rel Core) Fo_{99}	EPMA [6]	41.19	0.05	0.02	0.07	9.87	0.17	0.04	49.98	0.18	–	–	101.56
		(0.31)	(0.01)	(0.01)	(0.03)	(1.39)	(0.03)	(0.01)	(1.02)	(0.02)			
Silicate matrix	EPMA [8]	35.68	0.09	1.64	0.44	33.81	0.23	0.47	25.38	0.67	–	–	98.41
		(1.34)	(0.03)	(0.63)	(0.18)	(5.55)	(0.04)	(0.59)	(4.67)	(0.64)			
Px (Rel) $En_{99}Fs_1$	EPMA [10]	59.25	0.18	0.90	0.50	1.01	0.07	–	39.19	0.53	–	–	101.62
		(0.01)	(0.01)	(0.07)	(0.04)	(0.12)	(0.01)		(0.11)	(0.05)			
Ca-Px (Rel) $En_{67}Wo_{32}$	EPMA [2]	54.78	0.96	3.02	0.88	1.00	0.14	–	24.28	15.99	–	–	101.05
Nepheline	SEM-EDS [2]	42.7	–	35.8	–	–	–	–	–	3.4	15.6	1.3	98.8

Abbreviations: Ol, olivine; Rel, relict.

TABLE 3. Electron microprobe WDS analyses (wt% of oxides) of the Ca-phosphates.

Avg [*n.* spots] (SD)	SiO_2	FeO	MgO	CaO	Na_2O	P_2O_5	SO_3	SrO	BaO	Cl	Total
[5]	1.15	4.29	2.17	46.82	0.35	38.69	1.00	0.01	0.12	0.51	95.11
	(0.92)	(1.97)	(0.96)	(4.25)	(0.25)	(1.70)	(0.44)	(0.01)	(0.08)	(0.45)	

Fe-bearing (Fa_{78}). Intersecting curved fractures cut across the crystals and are partly filled by magnetite. In some veins, cavities are present with magnetite occurring as drusy layers along the vein wall (Figure 3b). Adjacent to the fractures, olivine is Fe-bearing. It shows zonation of forsterite (Fa_{99}) away from the fractures over 7 μm. The clast also has numerous irregular cavities, mostly in interstitial areas. In one region, olivine grains are nearly polyhedral (equant with 120° grain boundaries). Dusty olivines, which were disseminated in the matrix of FB-A1 (Agrosì et al., 2025), are not present in FB-A2.

At the boundary between the clast and the matrix, Fe-rich olivine embays phenocrysts. Around pyroxene, the Fe-rich olivine penetrates into the crystal by up to ~8 μm, forming parallel lamellae (Figure 3d). This suggests the Fe-rich rims are reaction rims and their morphologies are crystallographically controlled. Some olivine crystals also show fayalitic olivine areas as irregular cross-cutting lamellae, resembling flame perthite. In some crystals, these lamellae-bearing regions are only present along the exterior of the crystal (Figure 3b). In one area, in the center of the particle, the lamellae-bearing olivine is brecciated into angular clasts, <20 μm in size, with a matrix formed by magnetite. Lamellae within many of the clasts in the breccia match the orientation of those in neighboring clasts, indicating brecciation in situ.

TABLE 4. SEM-EDS analyses (wt% of elements) of sulfides on FB-A2a area.

Avg [*n.* spots] (SD)	S	Fe	Ni	Total
[3]	21.9	5.0	73.0	100
	(0.4)	(0.9)	(1.2)	

Small and finely aggregated crystals (0.2–1.1 μm in size) of phosphates, magnetite, Ni-bearing magnetite, and sulfides were also found on the pockets in the inner part of FB-A2b (Figure 3e) region and on its external rim (Figure 3a). Chemical (Table 3) and EBSD data (Figure S3) taken on the phosphates suggest that they mainly consist of whitlockite (Wht in Figure 3a). Although there is no trace of (Al,Cu)-alloys intermixed with silicates, tiny crystals containing Cu and Al are present on one edge. Their size is less than one micron, so it was not possible to analyze them in detail (Figures 3a and S4). Chemical analyses taken on sulfides reveal a pentlandite composition. It is worth noting that this composition is different from that of tiny crystals of sulfides disseminated in the glass of the FB-A2a area. The latter, in fact, show an S-undersaturated composition, in which the Ni content is substantially higher than the Fe content (heazlewoodite) (Tables 4 and 5).

TABLE 5. SEM-EDS analyses (wt% of elements) of sulfides on FB-A2b area.

Avg [*n*. spots] (SD)	S	Fe	Ni	Total
[4]	34.2 (1.4)	44.6 (7.3)	21.1 (6.1)	100

To confirm the extraterrestrial nature of FB-A2, secondary ion mass spectrometry $^{18}O/^{16}O$ and $^{17}O/^{16}O$ measurements were taken on the relict phenocrystals of olivine and pyroxenes (Figure 3). The acquired data show $\delta^{18}O$ values of −6.6 to −0.48 (0.19 to 0.61 uncertainties at 2σ) and $\delta^{17}O$ values of −6.6 to −0.48 (0.19 to 0.61 uncertainties at 2σ). The resulting oxygen isotope compositions, like the (Al,Cu)-bearing micrometeorites previously described (Agrosì et al., 2025; Bindi et al., 2025; Genge et al., 2025; MacPherson et al., 2013; Suttle et al., 2019), lie along the Carbonaceous Chondrite Anhydrous Mineral Line (the CCAM), confirming that FB-A2 is extraterrestrial (Figure 4).

DISCUSSION

The extraterrestrial origin of FB_A2 can be conclusively demonstrated by its oxygen isotope and chemical composition. The oxygen isotope ratios acquired on the relict phenocrysts of forsterite and pyroxene, lie on the CCAM line and away from the Terrestrial Fractionation Line, outside of uncertainty. The bulk chondritic composition of the particle likewise supports this extraterrestrial origin since terrestrial igneous rocks have very different chemical systematics. The presence of relict olivines and pyroxenes, disseminated in the Fe-rich silicate matrix, the external magnetite rim, which partially surrounds the fragment, and the presence of Fe-Ni metals, represent further evidence for its extraterrestrial origin (Genge et al., 2008). Furthermore, the presence of a magnetite rim suggests it formed as a micrometeorite—an object that was in space as a dust-sized particle, rather than a meteorite, since although meteorite fusion crust can have magnetite-rims (e.g. Genge et al., 2024) they are only found on the outer surface of the fusion crust rather than surrounding a particle (Genge et al., 2008). Finally, FB_A2 can be shown to be a micrometeorite rather than meteorite ablation debris, owing to the significant depletion of Na, relative to CI chondrite, within the fine-grained vesicular portions. Meteorite fusion crusts, the source of ablation debris, and airburst particles, formed during terminal detonations of larger meteoroids, both retain appreciable Na (Genge & Grady, 1999; Genge et al., 2024; van Ginneken et al., 2010, 2021).

Like the previously discovered FB-A1, FB-A2 shows the presence of (Al,Cu)-alloys within a chondritic mixture of silicates. However, the two micrometeorites show several different features. The irregular morphology of FB-A2 is substantially different from the sub-spherical shape of FB-A1 (Agrosì et al., 2025), which was rounded, testifying to a different degree of heating suffered during the atmospheric entry. The slightly elongated shape of FB-A1 is likely caused by aerodynamic shaping of a partially melted body during atmospheric passage, combined with surface tension. The (Al,Cu)-alloys in FB-A1 occurred in the form of veins modified by partial melting and show different copper contents along the elongation axis (Agrosì et al., 2025). The aforementioned characteristics, along with the presence of protrusions of metallic droplets on the external part of the FB-A1, corroborate the hypothesis that the (Al,Cu)-alloys suffered a near complete melting during the atmospheric entry, followed by rapid cooling.

The chondritic components in FB-A1 underwent extensive partial melting, as testified by (i) the presence of relict phenocrysts of forsteritic olivine disseminated in an amorphous matrix, (ii) the magnetite rim formed during the deceleration at high altitudes, and (iii) the high vesicularity related to degassing of volatiles. Particle FB-A1 was thus classified as a scoriaceous micrometeorite (Genge et al., 2008), albeit one that had experienced sufficiently high temperatures to begin forming a cosmic spherule. Conversely, the irregular morphology of FB-A2 implies little influence of melt surface tension on the shape, except in the vesicular areas with a smooth, lobate surface. Other areas have irregular shapes, suggesting low degrees of partial melting. Particle FB-A2 can thus also be classified as scoriaceous; however, it was heated significantly less than FB-A1 and is close to being an unmelted micrometeorite (Genge et al., 2008).

The presence of pyroxenes, nepheline, and Ca-phosphates in FB-A2, which were not found in FB-A1, along with the different matrix compositions, suggests both less heating in the atmosphere and a different pre-atmospheric protolith. In particular, the Ca-pyroxene normative composition of the FB-A1 matrix could be the result of complete melting of relict phenocrysts of pyroxenes, while in the FB_A2 matrix analyses suggest olivine normative compositions. The presence of nepheline in FB-A2 suggests affinities to CV3 and CO3 carbonaceous chondrites, where it is commonly found as fine grains in refractory inclusions and chondrules. The presence of nepheline in these meteorites is primarily ascribed to the replacement of melilite and plagioclase in refractory inclusions and plagioclase and glass in chondrules during metasomatism (Ichimura et al., 2017; Tomeoka & Itoh, 2004). This retention of Na in FB-A2 is

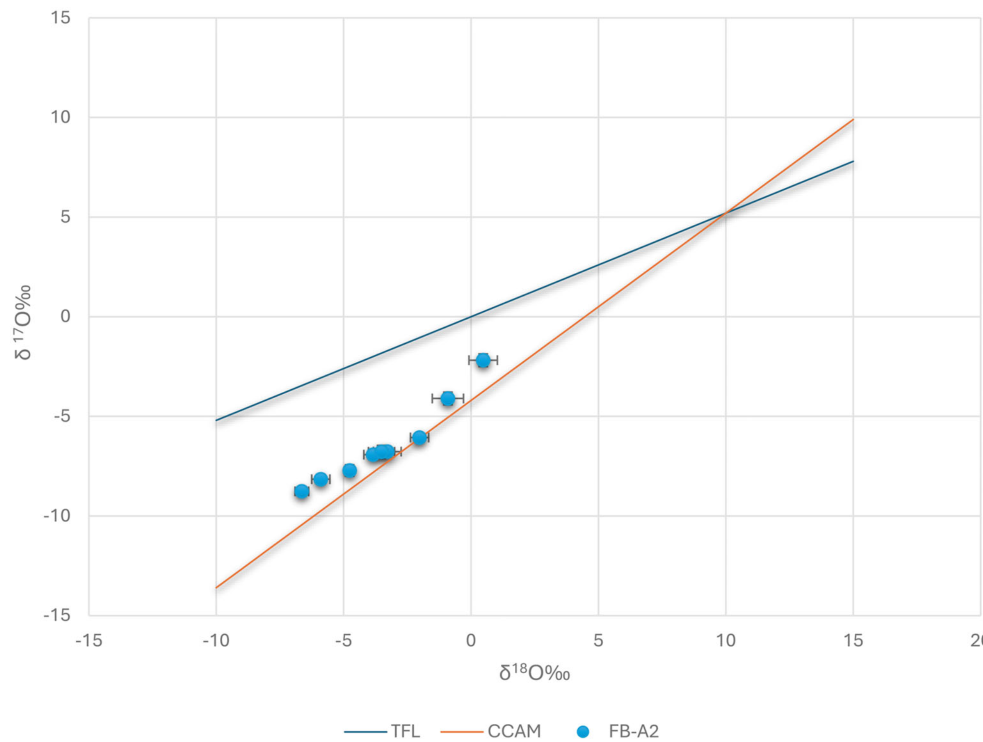

FIGURE 4. Plotted data were mainly taken on the relict olivine and pyroxene crystals of FB-A2 micrometeorite. The resulting oxygen isotope compositions lie along the line corresponding to anhydrous minerals in the CO or CV carbonaceous chondrites (the CCAM) and away from the Terrestrial Fractionation Line (TFL). (Color figure can be viewed at wileyonlinelibrary.com)

consistent with less evaporation than FB-A1 during atmospheric entry (Masiero et al., 2021).

Particle FB-A2 also contains phosphates, which have only rarely been reported in micrometeorites (Genge et al., 2008). In carbonaceous chondrites, phosphates represent secondary minerals formed through the chemical reaction of water with primary nebular solids on primitive asteroids from which these meteorites originated. In FB-A2, the occurrence of phosphates mixed with Ni-rich metal and sulfides in rounded masses represents a characteristic feature of phosphorus found in its oxidized form, a typical feature of an oxidized CV3 chondrite such as Khatyrka (MacPherson et al., 2013). These phases would likely be lost during the entry heating and melting of FB-A1, due to the decrease in stability of the hydrated phosphate phases during melting at temperatures of >1400 °C (Kizalaite et al., 2023).

Moreover, the intermixing of tiny crystals of phosphates (whitlockite) and sulfides (pentlandite) in cavities of brecciated area (FB-A2b) confirms further fluid-assisted metasomatism on the parent body. On the contrary, the presence of Ni-rich sulfides (heazlewoodite) in the FB-A2a region can be explained by intense localized heating with partial desulfurization and iron loss within the surficial sulfides during the impact event between the CV3 chondrite and a (Cu,Al) bearing body. Similar formation of heazlewoodite during atmospheric entry has been reported in meteorite fusion crusts (Genge et al., 2024).

The (Al,Cu)-alloys in FB-A2 are absent in the inner part of the micrometeorite. However, the analysis carried out on the unpolished sample revealed the presence of a large khatyrkite fragment with eutectoid morphology (presence of worm-like Cu-bearing aluminum), which implies a eutectic intergrowth of Al + $CuAl_2$ at a temperature of about 548 °C (Genge et al., 2025; Hollister et al., 2014). The lobate outlines of Cu-bearing aluminum in khatyrkite in FB-A1 were explained by melting during atmospheric entry followed by rapid cooling (Agrosì et al., 2025). The irregular shape of the (Al,Cu) alloy in FB_A2, however, testifies to minimal melting. Collectively, these features prove that FB-A2 underwent a lower degree of melting than FB-A1.

While FB-A1 records few primary features owing to significant atmospheric entry heating, particle FB-A2 records similar mineralogical and textural evidence to unmelted micrometeorite NG-1 and the Khatyrka meteorite for shock and a CV3 protolith (Genge et al., 2025; MacPherson et al., 2013). The oxygen isotope compositions of olivines and pyroxenes in FB-A2 are consistent with those from CV3 chondrites, like those in NG-1 and Khatyrka. The porphyritic clast in FB-A2, dominated by olivine and pyroxene phenocrysts with a glassy groundmass, is also consistent with CV3s and most likely represents a fragment of a Type-I chondrule since the phenocrysts have subhedral to euhedral shapes and the clast has an igneous texture. Chondrules have previously been reported in micrometeorites (Genge et al., 2006) and often form composite micrometeorites in which the fine-grained matrix has been melted to form an igneous rim (Genge, 2006), similar to the vesicular matrix observed in FB-A2. The normal zoning within the phenocrysts is significant, as it indicates an unequilibrated source similar to CV3 chondrites. Particle FB-A2 thus provides the first evidence in a micrometeorite that chondrules were present within the parent body of (Al,Cu)-alloy-bearing micrometeorites and suggests that they are derived from the same source as the Khatyrka meteorite.

The Khatyrka meteorite shows evidence for shock metamorphism and impact mixing of (Al, Cu)-alloy with the CV3 parent body. Similar evidence for shock is preserved in particle FB-A2 as curved, intersecting fractures and veins that cut olivine phenocrysts. Metal-sulfide veins are a common product of shock in chondrites (Ruzicka et al., 2015), and curved fractures typically form within shocked olivine (Stöffler et al., 1991). The area of the clast with polyhedral olivine with 120° grain boundaries can also be attributed to grain boundary formation within olivine owing to post-shock annealing (Stöffler et al., 1991). Lastly, it is worth noting that while Khatyrka shows high-pressure phases such as stishovite (Bindi et al., 2012), ahrensite (Hollister et al., 2014), and quasicrystals (Bindi, 2020), these phases are not observed within FB-A2. It is possible, however, that this is a sampling issue owing to the small size of FB-A2 since shock metamorphism is often spatially variable within chondrites (Stöffler et al., 1991).

Other features in FB-A2 are consistent with impact mixing of an (Al,Cu)-bearing projectile with the CV3 parent body. The zoned elongate olivine crystals within the fine-grained matrix of FB_A2 are similar to those observed in micrometeorite NG-1 and some samples of Khatyrka (Genge et al., 2025; MacPherson et al., 2013). MacPherson suggested this texture was a result of the mixing of CV3 matrix olivines, which have a characteristic bladed habit, with silicate shock melt. Furthermore, FeNi metal droplets seen in FB-A2 were observed concentrated in regions close to (Al,Cu)-alloy in both NG-1 and Khatyrka and form by reduction of the silicate melt (Genge et al., 2025; Lin et al., 2017).

While evidence for shock and mixing with CV3 materials are common between the Khatyrka meteorite, micrometeorite NG-1 and FB-A2, data from the current study also provides evidence for extreme disequilibria during the impact event. Olivine zonation around fractures within the chondrule fragment in FB-A2 have not previously been observed and suggest alteration of olivine by ingress of oxidizing gas or fluid. Although oxidation of silicates does occur during atmospheric entry, chemical diffusion within solid phases is slow at the relatively low temperatures at which FB-A2 likely experienced during atmospheric entry (600–800 °C). The heating pulse of micrometeorites during atmospheric flight is limited to a few tens of seconds, even at low entry angle (e.g., Genge, 2017) giving limited time for diffusion to occur. Reaction rims on pyroxene in FB-A2 might have formed during entry heating, however, usually these are present only around the exterior of relicts in scoriaceous micrometeorites (e.g., Genge et al., 2017). The penetration of Fe-rich olivine into pyroxenes along cleavage planes and fractures is not seen in other micrometeorites but is observed in CV3 chondrites as a result of parent body metasomatism (Brearley & Krot, 2013). Similarly, the lamellae networks observed within some olivines, in particular those forming zones along the outer margins of crystals, have similar textures to flame perthites formed by reaction replacement owing to metasomatism (Pandit, 2015). These olivines are thus consistent with the oxidative metasomatism that occurred during parent body alteration of oxidized CV3 chondrites.

Evidence for in situ brecciation of lamellae-bearing olivines is also observed in FB-A2, with clasts tens of microns in size surrounded by magnetite. Veins of magnetite that cross olivines connect with the magnetite containing the clasts. Metasomatic veins are observed within CV3 chondrites but contain assemblages of wollastonite, diopside, and andradite (Brearley & Krot, 2013). Furthermore, the alteration lamellae within olivine clasts are truncated, indicating that brecciation occurred after the peak in metasomatic alteration. Brecciation, together with the curved fractures within olivine, could occur owing to shock; however, Fe-rich shock veins usually comprise metal and sulfide (Ruzicka et al., 2015), but in FB-A2 include those with Ni-bearing magnetite. This provides an important constraint on the timing of the brecciation event, since if they result from shock, they must have formed during metasomatism to allow oxidation of metal-sulfide assemblages. Dating using Mn-Cr isotopes and thermodynamic modeling suggests that CV3 fayalite formation began 3.2 to 4.0 Myr after the formation of calcium-aluminum inclusions, and thus occurred in the early Solar System (Jogo et al., 2017). The duration of the event is uncertain, since it depends on the size of the CV3 parent body. For an object 200 km in diameter, metasomatic alteration could have continued for 10s of millions of years (Jogo et al., 2017). Brecciation could also be hydraulic in origin, resulting from fluid pressures that exceeded the tensile strength of forsterite (~12 GPa, Gouriet et al., 2025). Metasomatism of the oxidized CV3s is thought to have occurred owing to the ingress of fluids at temperatures of up to 540 °C, with fayalite principally forming at <300 °C and at pressures up to 30 MPa (Jogo et al., 2017). It is thus plausible that Ni-bearing magnetite could precipitate directly from metasomatic fluids; indeed, the cavities seen in magnetite veins in FB-A2 and drusy magnetite on vein walls are evidence for precipitation from a fluid. Evidence for hydraulic brecciation, however, is not commonly observed in CV3 chondrites, although metasomatic veins have been observed (Brearley & Krot, 2013), indicating pressures sufficient to cause fracture propagation. In situ fragmentation consistent with hydraulic brecciation has, however, been observed in the Winchcombe CM2 chondrite (Suttle et al., 2024).

Given that the bulk tensile strength of CV3 chondrites is significantly lower than that of olivine (10 MPa; Rubin, 1993), fluid pressures sufficiently high to fracture olivine (12 GPa) would also exceed the combination of the tensile strength of the rock and lithostatic pressure within a 200 km sized asteroid (>30 MPa at depths 27–60 km; Jogo et al., 2017), leading to disruption. Although some weakening of olivine may have occurred owing to metasomatism, allowing brecciation at lower overpressures, it thus seems likely that a local transient pressure excursion would be required to cause hydraulic brecciation of olivine without causing disruption of the parent body asteroid. Short-period pressure increases are likely to occur during impact events owing to shock wave propagation. Localized pressure excursions, furthermore, can occur owing to shock reverberation and interference, causing brecciation in restricted areas. Planar fabrics and lineations observed in CV3 chondrites have indeed been suggested to form by impacts and to influence the flow of metasomatic fluids (Tait et al., 2016). The evidence thus suggests that brecciation in FB-A2 testifies to an impact event during metasomatic alteration of the CV3 parent body in the early Solar System.

Two significant impact events thus appear to be recorded in FB-A2. One caused the brecciation of metasomatized olivines within the chondrule clast in the early Solar System. The second caused shock melting and mixing of elongate matrix olivines with shock melt. In particle NG-1 and Khatyrka, this second shock event appears to be associated with the delivery of (Al,Cu)-alloy (Genge et al., 2025). Lin et al. (2017) likewise found evidence for two impact events in Khatyrka, while Meier et al. (2018) found U, Th–He ages in olivine that suggest the second event occurred in the last 600 Ma.

The nature of metasomatism within the parent body of FB-A2 appears similar to that observed within oxidized CV3 chondrites such as Allende (CV3_OxA) owing to the formation of iron-rich olivines and presence of abundant magnetite. There is a consensus that metasomatism of CV3 chondrites is driven by high-temperature hydrous solutions, albeit one that can contain CO_2/CO and generate carbides at an early stage (e.g., Krot et al., 2025). No carbides were observed in FB-A2 to record this initial stage of alteration. Sulfides are present, but are not abundant in the particle suggesting fluids were sulfur-poor. Krot et al. (2025) underline that two types of magnetite are present in CV3: (1) "dirty" Cr-bearing magnetite, formed by the oxidation of FeNi metal in situ, and (2) "clean," Cr-poor magnetite that forms by precipitation from aqueous solutions. The magnetite within FB-A2 in brecciated areas is Cr-poor indicating precipitation.

Metasomatism within FB-A2 principally modal, replacing the primary mineralogy with iron-rich olivines, with only the Mg-rich cores of some larger olivine and pyroxene crystals preserved. However, the occurrence of veins, brecciated areas and lamellae appears to suggest a multi-stage processes in which cryptic and stealth metasomatism might have occurred, altering the chemistry and mineralogy of metasomatic products generated earlier. Whether this was in the form of discrete phases of metasomatism, or owing to evolving fluid composition and temperature, punctuated by shock events, cannot be determined since the small size of FB-A2 limits the wider textural and mineralogical constraints. Indeed, enhanced permeability and fluid mobility as a result of fragmentation is likely to result in changes in fluid compositions as locally buffered fluids mix with those derived from more distal sources.

The absence of phyllosilicates within FB-A2 differs from Bali-like oxidized CV3 chondrites (Krot et al., 1995, 1998) and is similar to Allende-type. In chondrites this has been attributed to the higher temperatures experienced by Allende-type CV3 chondrites, resulting in dehydration and removal of phyllosilicates (Krot et al., 2025). Micrometeorite FB-A2, however, has experienced atmospheric entry heating, with evidence for partial melting of silicates. Any phyllosilicates that might have been present prior to atmospheric entry would be become dehydroxlates at temperatures of (550–650 °C; Genge et al., 2008).

Another feature that distinguishes Khatyrka from micrometeorites is the presence of quasicrystals in the former (Bindi et al., 2012). Meteorites and micrometeorites, however, undergo different entry heating processes and thus different heating when crossing the atmosphere: the higher degree of heating suffered by micrometeorites may have caused the melting and recrystallization of metastable phases such as quasicrystals and high-pressure polymorphs into more stable crystal structures.

Particle FB-A2 is the sixth micrometeorite to date found to contain (Al,Cu)-alloy, while Khatyrka is the only meteorite known to contain the phase. All the micrometeorites with (Al,Cu)-alloy are from collections with minimal terrestrial ages, recovered from rooftops/gutters (Bindi et al., 2025; Genge et al., 2017, 2025), or from recent sedimentary sources such as Mount Gariglione (Agrosì et al., 2025) and the Sahara Desert (Suttle et al., 2019). These sedimentary micrometeorites show little evidence for terrestrial alteration emphasizing they have not been exposed to the terrestrial environment for an extended period of time (van Ginneken et al., 2017). Conversely, no (Al,Cu)-bearing particles have yet been recorded from Antarctic collections, many of which have accumulation ages of as much as 1 Ma, such as the Transantarctic Mountains collection (Rochette et al., 2008; Suavet et al., 2009), Cap Prudhomme (Genge et al., 1997, 2008; Maurette et al., 1991), Larkman Nunatak (Genge et al., 2018), and Dome Fuji (Noguchi & Takase, 2025). The absence of (Al,Cu)-alloy bearing micrometeorites from these collections might suggest that these particles are sampling a recent dust source in interplanetary space, such as a single asteroid that has experienced a collision event in the last few thousand years. The terrestrial residence age of the Khatyrka meteorite of 5000 yr provides a minimum estimate for the age of such an event (MacPherson et al., 2013), although transport times of meteorites and micrometeorites from the main belt can be 100 kyr to millions of years (Feige et al., 2024; Wieler & Graf, 2001).

Only two of the six (Al,Cu)-alloy-bearing micrometeorites have experienced minor heating during atmospheric entry, unmelted micrometeorite NG-1 (Genge et al., 2025) and the current particle FB-A2. All others are high-temperature scoriaceous or cosmic spherules. If statistically representative of the Earth's flux of (Al,Cu)-bearing micrometeorites, this may suggest these particles have higher entry velocities than average since greater heating is experienced at higher entry velocity (Love & Brownlee, 1991). This, in turn, would imply a higher eccentricity orbit (Genge, 2017), which would be consistent with a relatively recent source, since the orbits of dust particles in space become circularized over time by P-R light drag (Nesvorný et al., 2011). However, there is some evidence that suggests the current collection is not representative since although FB-A2 has experienced relatively little entry heating, it is very large (590 μm) and most particles of this size completely melt to form cosmic spherules. Only atmospheric entry at low entry angle and/or low entry velocity can survive without significant heating, contrary to the high abundance of (Al,Cu)-bearing cosmic spherules.

Particle FB-A2 represents a unique micrometeorite containing (Al,Cu)-alloy. It not only reinforces that micrometeorites and meteorites containing these alloys appear to come from a CV3 source, but also that the (Cu,Al)-alloy is derived from the projectile that collided with the CV3 parent body, which was suggested by Genge et al. (2025) to be the ureilite parent body. It also emphasizes that this group of unusual particles may be a relatively recent feature of Earth's extraterrestrial dust flux, which may consequently show more temporal variations in its sources than previously thought.

CONCLUSIONS

The discovery and detailed characterization of micrometeorite FB-A2 significantly advances our understanding of the origin, evolution, and delivery of (Al,Cu)-bearing extraterrestrial materials to Earth. FB-A2 provides the most complete microstructural and mineralogical record to date of the processes linking CV3 carbonaceous chondrites to exotic Al–Cu alloys, thereby strengthening the genetic connection between these micrometeorites, the unmelted particle NG-1 (Genge et al., 2025), and the Khatyrka meteorite (MacPherson et al., 2013).

FB-A2 demonstrates unequivocally that (Al,Cu)-bearing micrometeorites can preserve primary parent-body features, including chondrule fragments, metasomatic textures, and shock-related deformation. The identification of a porphyritic chondrule clast with unequilibrated olivine and pyroxene, combined with oxygen isotope compositions along the CCAM line, confirms a CV3-type source and shows that chondrules were present in the parent body of (Al,Cu)-alloy–bearing materials. This represents a critical step forward, as previous micrometeorites in this group were too strongly modified by atmospheric entry heating to retain such information.

Second, the textural relationships in FB-A2 provide compelling evidence for a complex, multi-stage impact history in the early Solar System. The coexistence of shock-induced fractures, metal–sulfide veins, polyhedral annealed olivine, metasomatic fayalite-rich lamellae, and in situ brecciation indicates that CV3 parent-body alteration, metasomatism, and impact processes were intimately linked. These observations support models in which transient pressure excursions during impacts enhanced fluid transport and oxidation during metasomatism, rather than metasomatism occurring in isolation under static conditions. FB-A2 thus offers rare micro-scale evidence that impacts actively shaped the chemical and mechanical evolution of oxidized CV3 parent bodies.

Third, FB-A2 reinforces the hypothesis that (Al,Cu)-alloys were not formed within the CV3 parent body itself but were introduced by impact mixing with an exotic projectile, most plausibly related to the ureilite parent body (Genge et al., 2025). The preservation of eutectoid Al–Cu textures and the spatial association of Fe–Ni metal droplets with the alloy mirror features observed in Khatyrka (Lin et al., 2017) and NG-1 (Genge et al., 2025) indicates a shared origin. FB-A2 therefore strengthens the emerging view that these alloys are tracers of violent collisional interactions between compositionally distinct planetesimals early in Solar System history.

Finally, the rarity and apparent youth of (Al,Cu)-bearing micrometeorites have broader implications for the temporal variability of the extraterrestrial dust flux at Earth. Their absence from long-residence Antarctic collections, combined with their presence in recent sedimentary and urban environments, suggests that they may derive from a relatively recent collisional event in the asteroid belt. If correct, this implies that the micrometeorite flux sampled at Earth can reflect short-lived, stochastic source events rather than a steady-state background alone.

In summary, FB-A2 bridges a critical gap between highly altered (Al,Cu)-bearing cosmic spherules and the Khatyrka meteorite. It provides the clearest evidence yet that these exotic alloys are part of a broader CV3-related collisional history involving impact mixing, metasomatism, and shock in the early Solar System. As such, FB-A2 highlights the unique power of micrometeorites to record processes that are otherwise only fragmentarily preserved in meteorites, offering a complementary and temporally sensitive archive of Solar System evolution.

Acknowledgments—The authors thank Francesco Badolato for providing the micrometeorite. The authors are also very grateful to Nicola Mongelli for the SEM-analyses performed at the University of Bari (Italy) and to Gioacchino Tempesta for the image acquisition shown in Figure 1a,b. Bruker Skyscan 1172 high-resolution μX-CT scanner has been purchased with funds from "PON Ricerca e Competitività 2007–2013." This study was conducted within the Space It Up project funded by the Italian Space Agency, ASI, and the Ministry of University and Research, MUR, under contract n. 2024-5-E.0-CUP n. I53D24000060005. Open access publishing facilitated by Universita degli Studi di Bari Aldo Moro, as part of the Wiley - CRUI-CARE agreement.

Conflict of Interest Statement—The authors declare that they have no known competing financial interests or personal relationships that could have appeared to influence the work reported in this paper.

Data Availability Statement—The data that support the findings of this study are available from the corresponding author upon reasonable request.

Editorial Handling—Michael Zolensky

REFERENCES

Agrosì, G., Manzari, P., Mele, D., Tempesta, G., Rizzo, F., Catelani, T., Cheng, G., Yao, N., Villeneuve, J., and Bindi, L. 2025. Unique (Al,Cu)-Alloys Discovered in a Micrometeorite from Southern Italy. *Communications Earth & Environment* 6: 271. https://doi.org/10.1038/s43247-025-02245-w.

Bindi, L. 2020. *Natural Quasicrystals, the Solar System's Hidden Secrets*. Switzerland: Springer. Springer Briefs. 96.

Bindi, L., Eiler, J., Guan, Y., Hollister, L. S., MacPherson, G. J., Steinhardt, P. J., and Yao, N. 2012. Evidence for the Extra-Terrestrial Origin of a Natural Quasicrystal. *Proceedings of the National Academy of Sciences of the United States of America* 109: 1396–1401. https://doi.org/10.1073/pnas.1111115109.

Bindi, L., Larsen, J., Kihle, J. B., Cheng, G., Hu, J., Yao, N., Ma, C., Guan, Y., Asimow, P. D., and Steinhardt, P. J. 2025. Metallic Messengers from the Cosmos: Rare (Al, Cu)-Bearing Meteorites from the Project Stardust Collection. *Meteoritics & Planetary Science* 60: 1609–20. https://doi.org/10.1111/maps.14377.

Bindi, L., Lin, C., Ma, C., and Steinhardt, P. J. 2016. Collisions in Outer Space Produced an Icosahedral Phase in the Khatyrka Meteorite Never Observed Previously in the Laboratory. *Scientific Reports* 6: 38117. https://doi.org/10.1038/srep38117.

Bindi, L., Steinhardt, P. J., Yao, N., and Lu, P. J. 2009. Natural Quasicrystals. *Science* 324: 1306–9. https://doi.org/10.1126/science.1170827.

Bindi, L., Steinhardt, P. J., Yao, N., and Lu, P. J. 2011. Icosahedrite, $Al_{63}Cu_{24}Fe_{13}$, the First Natural Quasicrystal. *American Mineralogist* 97: 881–84. https://doi.org/10.2138/am.2011.3758.

Brearley, A. J., and Krot, A. N. 2013. Metasomatism in the Early Solar System: The Record from Chondritic Meteorites. In *Metasomatism and the Chemical Transformation of Rock*. Lecture Notes in Earth System Sciences. Berlin, Heidelberg: Springer. https://doi.org/10.1007/978-3-642-28394-9_15.

Feige, J., Airo, A., Berger, D., Brückner, D., Gärtner, A., Genge, M., Leya, I., et al. 2024. Transport of Dust across the Solar System: Constraints on the Spatial Origin of Individual Micrometeorites from Cosmic-Ray Exposure. *Philosophical Transactions. Series A, Mathematical, Physical, and Engineering Sciences* 23: 382. https://doi.org/10.1098/rsta.2023.0197.

Genge, M. J. 2006. Igneous Rims on Micrometeorites. *Geochimica et Cosmochimica Acta* 70: 2603–21. https://doi.org/10.1016/j.gca.2006.02.005.

Genge, M. J. 2017. The Entry Heating and Abundances of Basaltic Micrometeorites. *Meteoritics & Planetary Science* 52: 1000–1013. https://doi.org/10.1111/maps.12830.

Genge, M. J., Alesbrook, L., Almeida, N., Bates, H. C., Bland, P. A., Almeida, N. V., Boyd, M. R., et al. 2024. The Fusion Crust of the Winchcombe Meteorite: A Preserved Record of Atmospheric Entry Processes.

Meteoritics & Planetary Science 59: 948–972. https://doi.org/10.1111/maps.13937.

Genge, M. J., Engrand, C., Gounelle, M., and Taylor, S. 2008. The Classification of Micrometeorites. *Meteoritics & Planetary Science* 43: 497–515. https://doi.org/10.1111/j.1945-5100.2008.tb00668.x.

Genge, M. J., Gileski, A., and Grady, M. M. 2006. Chondrules in Antarctic Micrometeorites. *Meteoritics & Planetary Science* 40: 225–238. https://doi.org/10.1111/j.1945-5100.2005.tb00377.x.

Genge, M. J., and Grady, M. M. 1999. The Fusion Crusts of Stony Meteorites: Implications for the Atmospheric Reprocessing of Extraterrestrial Materials. *Meteoritics & Planetary Science* 34: 341–356. https://doi.org/10.1111/j.1945-5100.1999.tb01344.x.

Genge, M. J., Grady, M. M., and Hutchison, R. 1997. The Textures and Compositions of Fine-Grained Antarctic Micrometeorites: Implications for Comparisons with Meteorites. *Geochimica et Cosmochimica Acta* 61: 5149–62. https://doi.org/10.1016/S0016-7037(97)00308-6.

Genge, M. J., Larsen, J., van Ginneken, M., and Suttle, M. D. 2017. An Urban Collection of Modern-Day Large Micrometeorites: Evidence for Variations in the Extraterrestrial Dust Flux through the Quaternary. *Geology* 45: 119–122. https://doi.org/10.1130/G38352.1.

Genge, M. J., Van Ginneken, M., Ma, C., Suttle, M. D., Almeida, N., Kita, N. T., Zhang, M., and Bindi, L. 2025. The First Al-Cu-Alloy-Bearing Unmelted Micrometeorite Suggests Contributions from the Disrupted Ureilite Protoplanet. *Earth and Planetary Science Letters* 656: 119276. https://doi.org/10.1016/j.epsl.2025.119276.

Genge, M. J., van Ginneken, M., Suttle, M. D., and Harvey, R. P. 2018. Accumulation Mechanisms of Micrometeorites in an Ancient Supraglacial Moraine at Larkman Nunatak, Antarctica. *Meteoritics & Planetary Science* 53: 2051–66. https://doi.org/10.1111/maps.13107.

Gouriet, K., Carrez, P., and Cordier, P. 2025. Ultimate Mechanical Properties of Forsterite. *Minerals* 9: 787. https://doi.org/10.3390/min9120787.

Hollister, L., Bindi, L., Yao, N., Hollister, L. S., Poirier, G. R., Andronicos, C. L., MacPherson, G. J., et al. 2014. Impact-Induced Shock and the Formation of Natural Quasicrystals in the Early Solar System. *Nature Communications* 5: 4040. https://doi.org/10.1038/ncomms5040.

Hu, J., Asimow, P. D., Ma, C., and Bindi, L. 2020. First Synthesis of a Unique Icosahedral Phase from the Khatyrka Meteorite by Shock-Recovery Experiment. *IUCrJ* 7: 434–444. https://doi.org/10.1107/S2052252520002729.

Ichimura, S., Seto, Y., and Tomeoka, K. 2017. Nepheline Formation in Chondrite Parent Bodies: Verification through Experiments. *Geochimica et Cosmochimica Acta* 210: 114–131. https://doi.org/10.1016/j.gca.2017.04.025.

Jogo, K., Nakamura, T., Ito, M., Wakita, S., Zolotov, M. Y., and Messenger, S. R. 2017. Mn–Cr Ages and Formation Conditions of Fayalite in CV3 Carbonaceous Chondrites: Constraints on the Accretion Ages of Chondritic Asteroids. *Geochimica et Cosmochimica Acta* 199: 58–74. https://doi.org/10.1016/j.gca.2016.11.027.

Kizalaite, A., Klimavicius, V., Balevicius, V., Niaura, G., Salak, A. N., Yang, J. C., Cho, S. H., Goto, T., Sekino, T., and Zarkov, A. 2023. Dissolution–Precipitation Synthesis and Thermal Stability of Magnesium Whitlockite. *CrystEngComm* 25: 4370–79. https://doi.org/10.1039/D3CE00602F.

Krot, A. N., Pataev, M. I., Piani, L., Marrochi, Y., Fujiya, W., Pravdivtseva, O. V., et al. 2025. Metasomatic Alteration of Type 3 Ordinary and Carbonaceous Chondrites. *Space Science Reviews* 221: 7. https://doi.org/10.1007/s11214-025-01135-z.

Krot, A. N., Scott, E. R. D., and Zolensky, M. E. 1995. Mineralogic and Chemical Variations among CV3 Chondrites and their Components: Nebular and Asteroidal Processing. *Meteoritics* 30: 748–775.

Krot, A. N., Zolensky, M. E., Keil, K., Scott, E. R. D., and Nakamura, K. 1998. Secondary Ca-Fe-Rich Minerals in the Bali-Like and Allende-Like Oxidized CV3 Chondrites and Allende Dark Inclusions. *Meteoritics and Planetary Science* 33: 623–645.

Larsen, J. 2017. *In Search of Stardust: Amazing Micrometeorites and their Terrestrial Imposters*. Oslo, Norway: Voyageur Press.

Lin, C., Hollister, L. S., MacPherson, G. J., Bindi, L., Ma, C., Andronicos, C. L., and Steinhardt, P. J. 2017. Evidence of Cross-Cutting and Redox Reaction in Khatyrka Meteorite Reveals Metallic-Al Minerals Formed in Outer Space. *Scientific Reports* 7: 1637. https://doi.org/10.1038/s41598-017-01445-5.

Love, S. G., and Brownlee, D. E. 1991. Heating and thermal transformation of micrometeoroids entering the Earth's atmosphere. *Icarus* 89(1): 26–43. ISSN 0019-1035. https://doi.org/10.1016/0019-1035(91)90085-8.

Ma, C., Hu, J., Suttle, M. D., Guan, Y., Sharp, T. G., Asimow, P. D., Steinhardt, P. J., and Bindi, L. 2023. Al-Cu-Fe Alloys in the Solar System: Going inside a Khatyrka-Like Micrometeorite (KT01) from the Nubian Desert, Sudan. *Meteoritics & Planetary Science* 58: 1642–53. https://doi.org/10.1111/maps.14089.

MacPherson, G. J., Andronicos, C. L., Bindi, L., Distler, V. V., Eddy, M. P., Eiler, J. M., Guan, Y., et al. 2013. Khatyrka, a New CV3 Find from the Koryak Mountains, Eastern Russia. *Meteoritics & Planetary Science* 48: 1499–1514. https://doi.org/10.1111/maps.12170.

Masiero, J. R., Davidsson, B. J. R., Liu, Y., Moore, K., and Tuite, M. 2021. Volatility of Sodium in Carbonaceous Chondrites at Temperatures Consistent with Low-Perihelion Asteroids. *The Planetary Science Journal* 2: 165. https://doi.org/10.3847/PSJ/ac0d02.

Maurette, M., Olinger, C., Michel-Levy, M., Kurat, G., Pourchet, M., Brandstätter, F., and Bourot-Denise, M. 1991. A Collection of Diverse Micrometeorites Recovered from 100 Tonnes of Antarctic Blue Ice. *Nature* 351: 44–47. https://doi.org/10.1038/351044a0.

Meier, M. M. M., Bindi, L., Heck, P. R., Neander, A. I., Spring, N. H., Riebe, M. E. I., Maden, C., et al. 2018. Cosmic History and a Candidate Parent Asteroid for the Quasicrystal-Bearing Meteorite Khatyrka. *Earth and Planetary Science Letters* 490: 122–131. https://doi.org/10.1016/j.epsl.2018.03.025.

Nesvorný, D., Janches, D., Vokrouhlický, D., Pokorný, P., Bottke, W. F., and Jenniskens, P. 2011. Dynamical Model for the Zodiacal Cloud and Sporadic Meteors. *The Astrophysical Journal* 743: 129. https://doi.org/10.1088/0004-637X/743/2/129.

Noguchi, T., Tominaga, T., Takase, M., Yamaguchi, A., and Imae, N. 2025. Collection of Antarctic Micrometeorites Stored in the Surface Snow near the Dome Fuji Station. *Meteoritics & Planetary Science* 60: 701–716.

Pandit, D. 2015. Geochemistry of Feldspar Intergrowth Microtextures from Paleoproterozoic Granitoids in Central India: Implications to Exsolution Processes in Granitic System. *Journal Geological Society of India* 85: 163–182. https://doi.org/10.1007/s12594-015-0204-9.

Rochette, P., Folco, L., Suavet, C., van Ginneken, M., Gattacceca, J., Perchiazzi, N., Braucher, R., and Harvey, R. P. 2008. Micrometeorites from the Transantarctic Mountains. *Proceedings of the National Academy of Sciences of the United States of America* 105: 206–211. https://doi.org/10.1073/pnas.0806049105.

Rubin, A. E. 1993. Dikes Vs. Diapirs in Viscoelastic Rock. *Earth and Planetary Science Letters* 117: 653–670. https://doi.org/10.1016/0012-821X(93)90109-M.

Ruzicka, A., Brown, R., Friedrich, J., Hutson, M., Hugo, R., and Rivers, M. 2015. Shock-Induced Mobilization of Metal and Sulfide in Planetesimals: Evidence from the Buck Mountains 005 (L6 S4) Dike-Bearing Chondrite. *American Mineralogist* 100: 2725–38. https://doi.org/10.2138/am-2015-5225.

Stöffler, D., Keil, K., and Scott, E. R. D. 1991. Shock Metamorphism of Ordinary Chondrites. *Geochimica et Cosmochimica Acta* 55: 3845–67. https://doi.org/10.1016/0016-7037(91)90078-J.

Suavet, C., Gattacceca, J., Rochette, P., Perchiazzi, N., Folco, L., Duprat, J., and Harvey, R. P. 2009. Magnetic Properties of Micrometeorites. *Journal of Geophysical Research Letters* 114: B04102. https://doi.org/10.1029/2008JB005831.

Suttle, M., Twegar, K., Nava, J., Spiess, R., Spratt, J., Campanale, F., and Folco, L. 2019. A Unique CO-Like Micro Meteorite Hosting an Exotic Al-Cu-Fe-Bearing Assemblage—Close Affinities with the Khatyrka Meteorite. *Scientific Reports* 9: 12426. https://doi.org/10.1038/s41598-019-48937-0.

Suttle, M. D., Daly, L., Jones, R. H., Jenkins, L., Ginneken, M., Mitchell, J. T., Bridges, J. C., et al. 2024. The Winchcombe Meteorite—A Regolith Breccia from a Rubble Pile CM Chondrite Asteroid. *Meteoritics & Planetary Science* 59: 1043–67. https://doi.org/10.1111/maps.13938.

Tait, A. W., Fisher, K. R., Srinivasan, P., and Simon, J. I. 2016. Evidence for Impact Induced Pressure Gradients on the Allende CV3 Parent Body: Consequences for Fluid and Volatile Transport. *Earth and Planetary Science Letters* 454: 213–224. https://doi.org/10.1016/j.epsl.2016.09.015.

Tomeoka, K., and Itoh, D. 2004. Sodium-Metasomatism in Chondrules in CO3 Chondrites: Relationship to Parent Body Thermal Metamorphism. *Meteoritics & Planetary Science* 39: 1359–73. https://doi.org/10.1111/j.1945-5100.2004.tb00951.x.

van Ginneken, M., Goderis, S., Artemieva, N., Debaille, V., Decrée, S., Harvey, R. P., Huwig, K. A., et al. 2021. A Large Meteoritic Event Over Antarctica ca. 430 ka Ago Inferred from Chondritic Spherules from the Sør Rondane Mountains. *Science Advances* 7: eabc1008. https://doi.org/10.1126/sciadv.abc1008.

van Ginneken, M., Folco, L., Perchiazzi, N., Rochett, e. P., and Bland, P. A. 2010. Meteoritic Ablation Debris from the Transantarctic Mountains: Evidence for a Tunguska-Like Impact over Antarctica ca. 480 ka Ago. *Earth and Planetary Science Letters* 293: 104–113. https://doi.org/10.1111/maps.12011.

van Ginneken, M., Genge, M. J., Folco, L., and Harvey, R. P. 2017. The Weathering of Micrometeorites from the Transantarctic Mountains. *Geochimica et Cosmochimica Acta* 179: 1–31. https://doi.org/10.1016/j.gca.2015.11.045.

Wieler, R., and Graf, T. 2001. Cosmic Ray Exposure History of Meteorites. In *Accretion of Extraterrestrial Matter throughout Earth's History*, edited by B. Peucker-Ehrenbrink, and B. Schmitz. Boston, MA: Springer. https://doi.org/10.1007/978-1-4419-8694-8_13.

SUPPORTING INFORMATION

Additional supporting information may be found in the online version of this article.

Video S1. Video by micro-CT of 3D reconstruction of FB-A2. Note the red portions corresponding to the metallic alloys.

Figure S1. Video of 3D reconstruction of FB-A2. Note the red portions corresponding to the metallic alloys.

Figure S2. FB-A2. Chemical maps of polished surface.

Figure S3. EDS spectra taken on the rim characterized by an intermixing of sulfides, phosphates and Fe,Ni oxides. Note the EBSD pattern taken of Ca-phosphates that match whitlockite with MAD 0.57.

Figure S4. BSE enlarged detail of clast. Green circle surrounds the rim region with tiny crystals of (Al,Cu) alloys. See the EDS spectra acquired. The size of crystals didn't allow as to carry out quantitative microanalyses.

Table 1. Porosity measurements taken by μ-CT.

Table 2. EPMA-WDS data taken on oxides (spot size 1 μm).